

## REVIEW ARTICLE

# Performance of Dynamically Simulated Reference Patterns for Cross-Correlation Electron Backscatter Diffraction

Brian E. Jackson,<sup>1</sup> Jordan J. Christensen,<sup>1</sup> Saransh Singh,<sup>2</sup> Marc De Graef,<sup>2</sup> David T. Fullwood,<sup>1,\*</sup> Eric R. Homer,<sup>1</sup> and Robert H. Wagoner<sup>3</sup>

<sup>1</sup>Mechanical Engineering Department, Brigham Young University, Provo, UT 84602, USA

<sup>2</sup>Department of Materials Science and Engineering, Carnegie Mellon University, 5000 Forbes Avenue, Pittsburgh, PA 15213, USA

<sup>3</sup>Department of Material Science and Engineering, Ohio State University, 2041 College Rd, Columbus, OH 43210, USA

**Abstract:** High-resolution (or “cross-correlation”) electron backscatter diffraction analysis (HR-EBSD) utilizes cross-correlation techniques to determine relative orientation and distortion of an experimental electron backscatter diffraction pattern with respect to a reference pattern. The integrity of absolute strain and tetragonality measurements of a standard Si/SiGe material have previously been analyzed using reference patterns produced by kinematical simulation. Although the results were promising, the noise levels were significantly higher for kinematically produced patterns, compared with real patterns taken from the Si region of the sample. This paper applies HR-EBSD techniques to analyze lattice distortion in an Si/SiGe sample, using recently developed dynamically simulated patterns. The results are compared with those from experimental and kinematically simulated patterns. Dynamical patterns provide significantly more precision than kinematical patterns. Dynamical patterns also provide better estimates of tetragonality at low levels of distortion relative to the reference pattern; kinematical patterns can perform better at large values of relative tetragonality due to the ability to rapidly generate patterns relating to a distorted lattice. A library of dynamically generated patterns with different lattice parameters might be used to achieve a similar advantage. The convergence of the cross-correlation approach is also assessed for the different reference pattern types.

**Key words:** cross-correlation EBSD, simulated electron backscatter diffraction, dynamical electron scattering, kinematical EBSD simulation, HR-EBSD

## INTRODUCTION

The practice of using electron backscatter diffraction (EBSD) to analyze the microstructure of materials is a well-established methodology for determining grain orientation and crystal lattice structure (Wright, 1993; Schwartz et al., 2009). Most commonly, a Hough transform approach searches for lines in the EBSD pattern (EBSP) that correspond to orientations of planes in the crystal. Accuracy of the orientation determination is typically some fraction of a degree (Wright & Nowell, 2008; Wright et al., 2011). High-resolution (or “cross-correlation”) electron backscatter diffraction (HR-EBSD) analysis, on the other hand, promised orientation precision that is several orders of magnitude better than Hough techniques (Troost et al., 1993; Wilkinson et al., 2006; Kacher et al., 2009). This approach compares an experimental pattern with some reference pattern by comparing sub-regions of the two patterns, referred to hereafter as regions of interest (ROI). Application of cross-

correlations, using fast Fourier transforms, determines the shifts necessary to align the matching ROI. These shifts are then used to calculate the relative distortion tensor between the lattices of the experimental and reference patterns. The relative orientation and strain between the experimental and reference lattices can then be extracted (Troost et al., 1993; Wilkinson et al., 2006; Villert et al., 2009). Furthermore, if the relative distortion is determined between adjacent scan points, the geometrically necessary dislocation content can be inferred (Landon et al., 2008; Gardner et al., 2010; Wilkinson & Randman, 2010; Ruggles & Fullwood, 2013).

Within the HR-EBSD technique exist two fundamental approaches for selecting the reference pattern: the first uses an experimental pattern from the same scan as the pattern of interest, whereas the second uses a simulated reference pattern. The use of an experimental, or “real,” reference pattern has been the more common approach due to the difficulty of accurately replicating microscope geometry when creating simulated patterns (Britton & Wilkinson, 2012; Alkorta, 2013). As the reference pattern comes from the same microscope arrangement, reasonable errors or

Received April 29, 2016; accepted June 29, 2016

\*Corresponding author. dfullwood@byu.edu

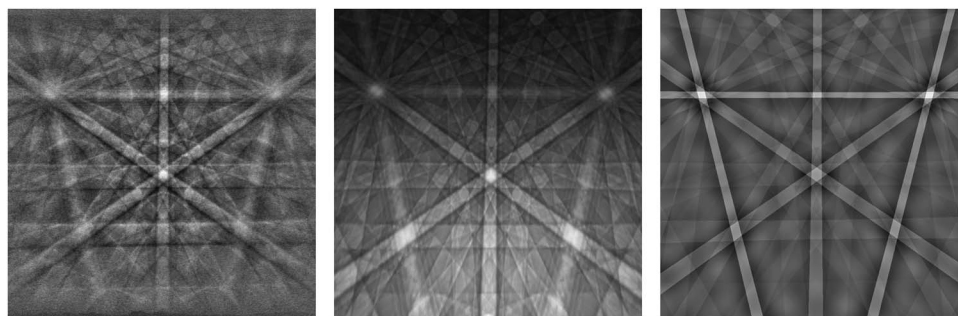


**Figure 1.** Electron backscatter diffraction patterns for silicon from experimental methods (left), dynamical simulation (middle), and kinematical simulation (right). No filtering or post-processing was applied to either the experimental or the dynamical simulation. The kinematical pattern used standard fast Fourier transform-type filtering to smooth the sharp details of the Bragg's law approach.

uncertainty in microscope geometry can be tolerated in the determination of relative distortion. However, as the absolute strain and orientation of the reference pattern are unknown, only relative measurements can be performed when using this approach. The use of a simulated reference pattern promises to overcome this limitation, as the absolute strain and orientation of the reference pattern are known exactly. If the microscope geometry (and other factors that introduce noise into the measurement) can be adequately determined, this enables the calculation of absolute strain or distortion for the experimental lattice. In addition, the use of simulated reference patterns potentially offers higher accuracy orientation measurements, resolution of orientation for noisy patterns, and resolution of pseudo symmetry (Winkelmann et al., 2007; Kacher et al., 2009; Callahan & De Graef, 2013).

Accurate pattern center (PC, i.e., microscope geometry) determination is the most significant challenge when using a simulated reference. The PC is defined as the point where the backscattered electrons impinge normal to the scintillator surface. An inaccurate PC will cause the simulated pattern to be artificially shifted relative to the experimental pattern, which will result in phantom strain and tetragonality. Various methods have been explored to accurately determine the PC, but it still remains a major obstacle when using simulated reference patterns (Britton et al., 2010; Basinger et al., 2011; Alkorta, 2013).

Currently, two methods have been used to create simulated EBSD: kinematical diffraction and dynamical diffraction. The kinematical approach relies on Bragg's law to correctly determine the Kikuchi band positions. Kinematically simulated EBSD are generally simplistic, and suffer from nonrealistic representations of band intensity profiles and other characteristics of experimental patterns (Kacher et al., 2010; Fullwood et al., 2015). Dynamically simulated patterns, on the other hand, start from a computationally intensive Monte Carlo (MC) simulation of the energy, depth, and directional distributions of backscattered electrons and use this information to dynamically simulate a master EBSD covering all orientations (Callahan & De Graef, 2013); this master pattern is then used as a library to extract, via bilinear interpolation, an EBSD for a given

detector geometry and sample orientation. Dynamically simulated patterns better reproduce the characteristics of experimental patterns than kinematically simulated patterns (see Fig. 1) (Winkelmann et al., 2016). In either case, an iterative approach is typically applied to align the simulated pattern more closely with the pattern of interest (Kacher et al., 2009; Fullwood et al., 2015).

The purpose of the current study is to compare the accuracy and precision of strain and tetragonality measurements using kinematically and dynamically simulated reference patterns for a standard material with a known tetragonality. The influence of PC error is analyzed for both types of simulated patterns. In addition, the effect of using an iterative cross-correlation analysis approach for both kinematically and dynamically simulated reference patterns is also examined.

## MATERIALS AND METHODS

### Samples and Data Collection

The samples used in the current study are described in detail by Vaudin et al. (2015). The nomenclature and coordinate system used in Fullwood et al. (2015) are adopted in this paper for consistency. Various thicknesses of epitaxial layers of  $\text{Si}_{1-x}\text{Ge}_x$  were deposited on 300 mm Si wafers at different compositions. Two samples were selected for the low uncertainty of the predicted and measured tetragonal distortion reported in Vaudin et al. (2015). The first scan, referenced in the current paper as S01, had a composition of 19.4% Ge and an  $\text{Si}_{1-x}\text{Ge}_x$  film thickness of 47.4 nm. The second scan, referenced as i02, had a composition of 27.9% and a thickness of 35.9 nm. Strips of the epitaxial  $\text{Si}_{1-x}\text{Ge}_x$  were etched away, exposing thin strips of bare silicon between mesas of  $\text{Si}_{1-x}\text{Ge}_x$ .

The EBSD were collected using a commercial EBSD system (HKL Nordlys II; Oxford Instruments, Abingdon, UK) installed on a cold tip field-emission gun SEM (Hitachi model 4700; Japan), operated at an accelerating voltage of 20 kV with a probe current, as measured by a Faraday cup of about 2 nA. A line scan of 250–280 points,

with a step size of  $1\ \mu\text{m}$ , was taken across multiple  $\text{Si}_{1-x}\text{Ge}_x$  mesas. The samples were tilted at  $70^\circ$  from the horizontal, and the phosphor screen normal was held at  $0^\circ$  with respect to the horizontal. The patterns were recorded at a resolution of  $1,344 \times 1,024$  pixels with 8 bit intensity resolution and integration times of about 1 s/point.

## Simulated Pattern Generation

### *Kinematical EBSP*

Kinematical EBSPs are based on Bragg's law:

$$2d_{hkl}\sin\theta = m\lambda, \quad (1)$$

which defines positions for which constructive interference of scattered electrons (of wavelength  $\lambda$ ) occurs from planes with interplanar spacing  $d_{hkl}$  ( $hkl$  are the Miller indices of the lattice planes). For each set of lattice planes, two conical surfaces of angle  $\theta$  with respect to the plane define a volume whose intersection with the detector surface produces a Kikuchi band on the EBSP. The integer  $m$  specifies the order of the diffraction band; as only first-order bands are used in our simulation,  $m$  is set to unity.

The details of the computation are described in Kacher et al. (2009). In summary, the simulation requires the crystal lattice information, sample tilt, elevation angle, phosphor screen size in pixels, PC, distance from sample to the phosphor screen, and the crystal orientation.

After the bands for each diffraction plane for the given lattice structure are computed and summed together, a bandpass filter is applied to the simulated image to improve the similarity with real patterns at band axes. Although the band positioning for this simplistic simulation is good, the approach suffers from poor band profile and intensity replication, especially at band axes.

Due to the simplistic nature of the computation, patterns can be generated very quickly (about 1 s/pattern). Furthermore, in addition to the ability to modify the input orientation, the hypothetical lattice that defines the kinematical pattern can be distorted to accurately simulate a strained lattice without any time penalty. Therefore, an iterative approach can be used to modify the simulated image until it closely matches the experimental image in both orientation and strain (Fullwood et al., 2015). The convergence properties of this iterative approach, as well as the effect of including strain in the simulated pattern, are discussed in detail in a later section.

### *Dynamical EBSP*

The dynamical EBSP were generated using EMsoft 3.0 (De Graef, 2015), an open-source software package for simulation of electron diffraction and imaging modalities developed at Carnegie Mellon University. The generation of dynamical EBSP using EMsoft proceeds in three steps, described in detail in Callahan & De Graef (2013):

1. MC simulation of the energy, depth, and directional distributions of backscattered electrons.

2. Dynamical simulation of the EBSP master pattern, covering all possible backscattered electron directions with respect to the crystal lattice.
3. Simulation of an EBSP for a given detector geometry and sample (grain) orientation.

The MC simulation is used to compute the electron distribution in the hemisphere on the vacuum side of the sample surface; for computational convenience, the histograms resulting from the MC simulation are formatted as modified Lambert projections (Roşca & De Graef, 2013; Roşca et al., 2014). The MC simulation uses the continuous slowing down approximation, a coarse approximation which replaces complex scattering processes, such as core losses, outer shell excitations, plasmons, phonons, etc. by a constant energy loss rate (Joy, 1995). The simulation computes the trajectories of randomized individual electrons as they pass through the sample and undergo scattering events. The direction cosines, energy, and depth of the last scattering event are recorded for those electrons that leave the sample. The program output, in HDF5 format (The HDF Group, 2014), consists of the spatial distribution of electrons, represented on a modified Lambert projection, for each of a series of energy bins, as well as the depth distribution versus exit energy and orientation. The MC simulation is computationally intensive, and is carried out on a graphical processing unit (GPU) using the OpenCL approach; each MC run typically requires about 30 min to complete for  $2 \times 10^9$  incident electrons, although this time is strongly dependent on the type of graphics card used and can be as short as 6 min for the Nvidia Tesla K80 card. The MC simulation and subsequent steps of the dynamical EBSP generation utilize the latest techniques for accurate pattern simulation (Deal et al., 2008; Rice et al., 2014).

The following inputs are required for the MC simulation: crystal structure (lattice parameters, space group number, and atom positions in the asymmetric unit, including the site occupation parameters and Debye-Waller factors); sample orientation (described by two tilt angles with respect to the horizontal axis and the RD axis); the total number of incident electrons (typically  $10^9$ ); the number of electrons per thread (for GPU processing); the incident beam energy and the number and size of the histogram energy bins; and the depth range, bin size and number of bins for the depth histograms.

The output of the MC simulation is then used to create a dynamical master EBSP covering all possible directions. This step is computationally demanding as a master EBSP is generated for each energy bin. The pattern is generated by combining the Bloch wave dynamical scattering approach (Humphreys, 1979) with a depth integration using MC-derived weight factors and integration bounds (Callahan & De Graef, 2013). As the master pattern program uses the MC output, only two additional parameters are required as input: a Fourier space truncation value to limit the number of beams that are taken into account in the dynamical simulation, and the size of the master EBSP in

pixels. Typically both the MC and master EBSD simulations can both be performed in under 1 h on a typical multi-threaded workstation. MC and master EBSD simulations are unique to the material and lattice state (strained or strain free), so new simulations must be performed when either the material or lattice state changes. As microscope geometry is taken into account at the time of pattern generation, these simulations can be shared between EMsoft users.

After both MC and master pattern simulations have been completed, individual EBSP can be computed relatively quickly for a given sample (grain) orientation. In its current iteration, EMsoft generated these  $1,024 \times 1,024$  resolution patterns in about 1 s; however, in future releases the master EBSP can be loaded into memory, which will reduce this time to  $<0.5$  s/pattern. Using this approach, small patterns of about  $80 \times 60$  resolution patterns can be generated at a rate of about 500 patterns/s. The master EBSP is used as a look-up table (with appropriate bilinear interpolation) for the EBSD intensity for all pixel positions on the scintillator (phosphor) screen, once the necessary geometric transformations are applied for a given grain orientation. The resulting EBSP can then be compared directly with an experimental image. The generation of the final dynamical EBSP requires the following inputs: microscope parameters (camera tilt angle, charge-coupled device (CCD) pixel size at the scintillator, incident beam current, beam dwell time, and camera binning mode); EBSP parameters (pattern size in pixels, grain orientation, typically stated in Euler angle or quaternion form, the PC coordinates, and the distance between scintillator and illumination point); image parameters (intensity scaling mode, circular mask, and the energy integration range). At present, the final pattern generated by EMsoft 3.0 does not take into account the point spread function of the optics that projects the photons onto the CCD chip, Poisson noise, as well as any binning and contrast/brightness scaling that can be applied to the pattern using the vendor software.

## HR-EBSD

### Overview

The HR-EBSD analysis was performed using the proprietary open-access code, OpenXY, developed by Brigham Young University (2015). OpenXY allows HR-EBSD analysis with both experimental and simulated reference patterns. In its default configuration, OpenXY only utilizes kinematically simulated patterns, so for the purposes of comparing kinematical and dynamical patterns, EMsoft 3.0 was integrated with OpenXY. Although the core cross-correlation algorithm for comparing two patterns is the same for experimental, kinematical, and dynamical reference patterns, the overall approaches are distinct.

For all reference pattern types, a reference pattern is specified for each point in the sample. For experimental reference patterns, this can be a single pattern manually selected by its index number, or can be automatically selected from a centralized location in a grain. For simulated patterns, typically a new simulated reference pattern is generated for

each point in the sample (based upon orientation information estimated by the commercial software used in the initial scan). Each scan point is then compared using standard cross-correlation techniques with its reference pattern, and the deformation tensor is extracted.

For experimental reference patterns, the cross-correlation is performed only once, whereas for simulated reference patterns the cross-correlation is performed multiple times to iteratively find the best possible match between the experimental and simulated patterns. The rotational component of the distortion tensor resulting from the cross-correlation of the simulated reference pattern and the experimental pattern is used to modify the assumed orientation of the scan point, and this is used to generate a new simulated reference pattern (Landon et al., 2008; Kacher et al., 2009; Fullwood et al., 2015). This process is iterated several times, where the distortion tensor of the previous iteration is used to generate a new simulated reference pattern, which is in turn compared with the experimental pattern.

For the dynamical patterns, only the orientation adjustment required by the deformation tensor is currently used to produce the patterns for subsequent iterations. Although EMsoft can readily produce patterns for a strained lattice, this would require the production of a new master pattern each time, resulting in computation time of the order of hours rather than seconds. Hence it is impractical to iterate on lattice strain, at least in a general sense (several master files could be precomputed for a discrete set of known strains if desired). For kinematical patterns, arbitrary strains can readily be incorporated into the hypothetical lattice with no time penalty. Hence, once an optimal orientation is found, the entire deformation tensor is used to create a new strained reference pattern. This process is also iterated until the kinematical reference pattern closely matches the experimental pattern in both orientation and strain. See Figure 2 for a graphical representation of the cross-correlation approach. This iterative approach for kinematical patterns is discussed in detail by Fullwood et al. (2015). The convergence of this iterative algorithm, as well as the potential advantage of simulating a strained/tetragonal lattice using kinematical patterns, is discussed in a later section.

Modifications to the algorithm described in Fullwood et al. (2015) to accommodate the EMsoft environment are illustrated in Figure 3. The MC simulation and the master EBSP generation were performed for the given material before performing the HR-EBSD analysis. OpenXY was modified to set up the required environmental variables within the local Matlab environment, and check for the existence of the required MC and master EBSP output files. Each time a new dynamical pattern is generated, OpenXY modifies the name list file used by EMsoft's EMEBSD.f90 program with the orientation and PC information. The EMEBSD program is then called by OpenXY, the output hdf5 file is read, and the dynamical EBSP is extracted.



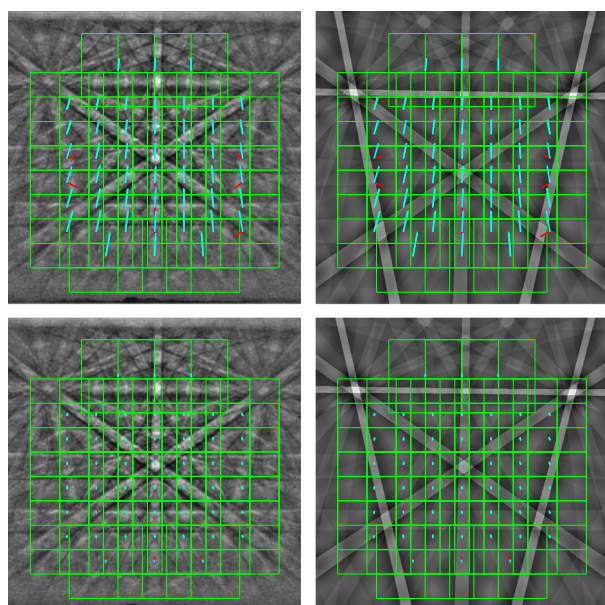


**Figure 2.** Experimental pattern (left column) and kinematically simulated reference pattern (right column) shown with regions of interest (ROI) and calculated shifts for each ROI, for one iteration (top row) and after several iterations (bottom row; shifts are scaled up by  $10\times$  to make them viewable). Note the decrease in the magnitude of shifts after several iterations. Red shifts are shifts whose magnitude and direction are  $>2$  SD from the mean of the shifts, and are excluded from the overall deformation tensor calculation.

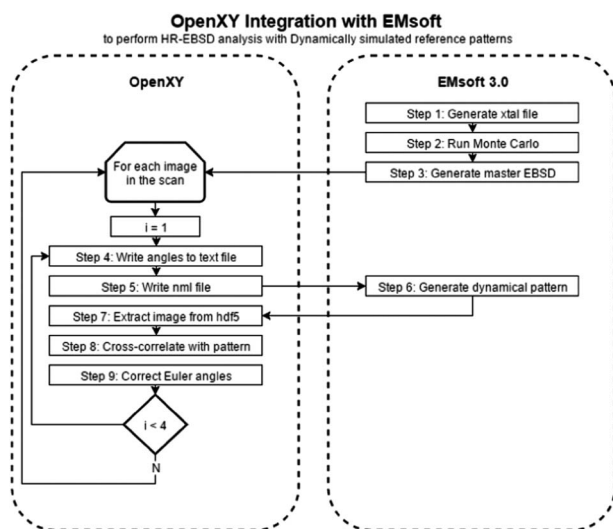


**Figure 3.** Overview of integration of OpenXY with EMsoft to perform high-resolution electron backscatter diffraction (HR-EBSD) analysis with dynamically simulated reference patterns.

### PC Determination

When an EBSD scan is performed, commercial software must estimate microscope geometry (PC) in order to correctly index (determine lattice orientation) for the resultant patterns. However, the resultant estimate is

generally too coarse to form the basis for simulated reference patterns (Fullwood et al., 2015). Various approaches are available for improving on the PC estimate, including Biggin & Dingley (1977), Basinger et al. (2011) Maurice et al. (2011), and Mingard et al. (2014). For the current study, the same strain-minimization technique used by Fullwood et al. (2015) was employed to determine the correct PC for each scan. The best PC was typically found by calibrating and averaging the PC for three points of high image quality from the third silicon band, which had a higher average image quality across the band than the other bands. Future studies will investigate more thoroughly the effect of image quality on the strain-minimization calibration technique used in the current study, as well as investigate other methods for reliably determining PCs.

It was initially expected that performing the PC calibration using either kinematically or dynamically simulated reference patterns should yield the same PC. However, using the strain-minimization approach, different PCs were found for kinematical and dynamical reference patterns. To investigate whether the discrepancy was persistent across all orientations, 64 simulated patterns with a known PC and different orientations were generated, using both kinematical and dynamical simulation approaches. The PC of the simulated series of dynamical images was calibrated using kinematical reference images, and vice versa. The results are shown in Table 1. When a simulated pattern was calibrated against a simulated pattern of the same kind (kinematical or dynamical), all fits resulted in a PC that was on average within  $4\mu\text{m}$  from the nominal PC, or one-fifth of a single pixel, and an average SD of  $5.5\mu\text{m}$ . These results show the reliability of the PC calibration method across a wide range of crystal orientations. When calibrating the PC using the other type of simulated pattern, however, the calibrated PC was an average of  $77\mu\text{m}$  away, with an average SD of  $30\mu\text{m}$ . This suggests that as the PC is independent of the orientation of the simulated reference image, the difference in PCs between dynamically and kinematically simulated patterns is due to the patterns themselves, and not an artifact of the algorithm. The exact cause of this discrepancy is still under investigation, but it is possible that the discrepancy is due to the differences in band intensities, band widths, and contrast of the patterns. For example, it was found that filtering the image had a noticeable effect on PC calibration. In the results below, the PC is recalibrated for each type of pattern being used as reference pattern.

### Sample Analysis

The two  $\text{Si/Si}_{1-x}\text{Ge}_x$  samples were analyzed according to the method outlined in the previous sections using both kinematical and dynamical reference patterns. For the initial comparisons between the accuracy obtained from kinematical and dynamical patterns, all settings in OpenXY were left at their default values. A grid pattern of 48 ROIs, at 25% of the scan image were used to perform the cross-correlation analysis (see Fig. 2) (Villert et al., 2009). It has been found

**Table 1.** Differences in Pattern Center Calibration for Different Simulated Pattern Types, Across Several Orientations for the  $x$ ,  $y$ , and  $z$  Components of the Pattern Center.

Calibration		Mean and SD of Differences		
Scan Type	Ref Image Type	X Star	Y Star	Z Star
Dynamical	Dynamical	$-1.68 \pm 10.53$	$-2.11 \pm 6.05$	$4.13 \pm 4.85$
Dynamical	Kinematical	$-79.18 \pm 47.44$	$-271.04 \pm 8.63$	$70.93 \pm 10.78$
Kinematical	Dynamical	$-24.55 \pm 35.05$	$-1.66 \pm 42.59$	$12.74 \pm 39.75$
Kinematical	Kinematical	$-6.37 \pm 6.92$	$-3.76 \pm 1.53$	$-5.41 \pm 2.22$

Units in  $\mu\text{m}$ .

that ROI selection has a significant impact on the results of the cross-correlation, and the grid method used in the current study produced the best results of the methods initially tested. It is suggested that future studies investigate more fully the impact of ROI selection and possible ROI optimization to reduce calculation time. Four analyses were performed on each scan, using (1) experimental reference patterns, (2) kinematically simulated reference patterns, (3) dynamically simulated reference patterns, and (4) a single dynamically simulated reference pattern for the entire scan, for direct comparison with experimental reference pattern method.

When using experimental reference images, a single reference image from the first silicon segment was selected for the entire scan. The fifth image of the scan was selected for both samples for consistency with previous studies (Fullwood et al., 2015). For kinematical patterns, three rotation-correction-only iterations were used, followed by six iterations including the strain component. Two analyses with dynamical patterns were performed, both using four rotation-correction-only iterations. The first analysis using dynamical patterns generated a new dynamical reference pattern for each scan point (based upon the orientation estimate derived by the commercial EBSD software), similar to kinematical patterns. The second analysis generated a single dynamical reference pattern using the fifth scan point, similar to the approach for experimental patterns. Total analysis time for both scans was about 40 min, which is significantly higher than typical EBSD analysis on a point-to-point basis due to the high resolution of the experimental pattern.

#### Comparison of Accuracy and Precision

After performing the cross-correlation analyses, the  $\epsilon_{11}$ ,  $\epsilon_{22}$ , and  $\epsilon_{33}$  strain components were extracted from the deformation tensor for each point and plotted. The tetragonality was calculated using the standard formula for tetragonality:

$$\epsilon^{\text{tet}} = \epsilon_{33}^{\text{crystal}} - \frac{\epsilon_{11}^{\text{crystal}} + \epsilon_{22}^{\text{crystal}}}{2}. \quad (2)$$

In order to quantitatively compare the results of using experimental versus kinematical versus dynamical reference patterns, both the accuracy and precision of the scans were

**Table 2.** Expected Tetragonality for the SiGe Regions of the Two Samples Used in this Study, from Vaudin et al. (2015).

S01	i02
$1.23 \pm 0.02$	$1.93 \pm 0.03$

compared. The accuracy was calculated by finding the sum of squared error (SSE) of the tetragonality. The actual tetragonality of the strain-free silicon was assumed to be 0, and that of the silicon germanium was assumed to be equal to the tetragonality measured by Vaudin et al. (2015) (see Table 2). It was observed in a previous study that kinematical patterns appear to be “noisier” than experimental patterns (Fullwood et al., 2015). The precision, which indicates this “noise” level, was measured using the standard deviation in silicon and silicon germanium for both strain and tetragonality.

#### Convergence of Iterative Algorithm

As mentioned previously, HR-EBSD analysis with simulated reference patterns uses an iterative approach to reduce the magnitude of the shifts between the simulated reference pattern and the experimental pattern, which has been shown to improve the accuracy of the cross-correlation (Kacher et al., 2009; Britton et al., 2010; Kacher et al., 2010; Maurice et al., 2010; Britton & Wilkinson, 2012). Although this approach has been used for some time, no investigation has been performed to determine the nature of the convergence of this iterative algorithm. A better understanding of how the algorithm converges will provide a measure of confidence in the final shifts determined by the algorithm, as well as potentially allow for optimization, so that the best results are achieved in the shortest amount of computation time.

The convergence was analyzed in terms of three metrics: the norm of the deformation tensor, a cross-correlation measure, and the average ROI shift magnitude at each iteration. The cross-correlation coefficient used was defined by Winkelmann (2010):

$$r = \frac{1}{n} \sum_{x,y} \frac{(f(x,y) - \bar{f})(t(x,y) - \bar{t})}{\sigma_f \sigma_t}, \quad (3)$$

where  $f$  and  $t$  are the same ROI in the reference and experimental pattern. The average of all the cross-correlation coefficients (taken over all ROIs) was recorded for each iteration.

The convergence of these values was tracked over various numbers of iterations. For the dynamical reference patterns, only orientation was adjusted at each iteration. For kinematical patterns, convergence of both the orientation-only adjustments, and orientation plus strain adjustments of the reference pattern were analyzed.

#### Impact of Simulating a Deformed Lattice

The reference dynamical patterns used throughout this paper were based upon cubic symmetry; as mentioned previously, the computational cost of generating dynamical patterns with an arbitrarily “strained” lattice is not practical. Hence it is assumed that at some level of lattice tetragonality, the cubic lattice symmetry used by the dynamical simulations will give poorer results than the arbitrarily strained lattice symmetry of the kinematical simulations. In order to quantify this effect, various dynamically simulated patterns were generated to simulate scans of tetragonal materials with varying levels of tetragonality. These scans were then analyzed using cubic dynamical patterns, and kinematical patterns with arbitrary deformation applied to the lattice. Hence the kinematical patterns were able to more accurately represent the original lattice structure.

To generate the hypothetical silicon germanium patterns, the base silicon crystal lattice was modified to achieve varying levels of tetragonality. As for the real material (Vaudin et al., 2015), it was assumed that  $\epsilon_{11} = \epsilon_{22}$ , and in line with the traction-free assumption made by the HR-EBSD algorithm, it was assumed that  $\epsilon_{11} = \epsilon_{22} - \epsilon_{33}$ , which gave the following relationships derived from the equation for tetragonality [equation (2)]:

$$\epsilon_{33} = \frac{\epsilon_{\text{tet}}}{2}, \quad (4)$$

$$\epsilon_{11} = -\frac{\epsilon_{\text{tet}}}{2}, \quad (5)$$

where  $\epsilon_{33}$  and  $\epsilon_{11}$  are given by

$$\epsilon_{33} = \frac{c_{\text{SiGe}} - a_{\text{Si}}}{a_{\text{Si}}}, \quad (6)$$

$$\epsilon_{11} = \frac{a_{\text{SiGe}} - a_{\text{Si}}}{a_{\text{Si}}}, \quad (7)$$

which results in the following equations for the lattice parameters of the tetragonal silicon lattice:

$$c_{\text{SiGe}} = a_{\text{Si}} \left( \frac{\epsilon_{\text{tet}}}{2} + 1 \right), \quad (8)$$

$$a_{\text{SiGe}} = a_{\text{Si}} \left( -\frac{\epsilon_{\text{tet}}}{2} + 1 \right). \quad (9)$$

The  $a_{\text{SiGe}}$  and  $c_{\text{SiGe}}$  lattice parameters were then used to generate a new MC simulation and master EBSD for each level of tetragonality, from which hypothetical scan images

were then generated. All images had the same orientation and PC, based upon averages from the S01 scan. In order to simulate tetragonality in the cubic silicon lattice structure, the lattice parameters were converted from the cubic 227  $\text{Fd}\bar{3}\text{m}$  space group to the tetragonal 141  $\text{I}4_1/\text{amd}$  space group. The  $a$  and  $b$  lattice parameters were divided by  $\sqrt{2}$  to take into account the  $45^\circ$  rotation about the  $c$  axis with respect to the cubic unit cell. A simulated scan with the same structure as the S01 scan was generated for each level of tetragonality, and a scan file was generated with the orientation and PC. Each scan was then analyzed using a “real” reference pattern—a single pattern selected from a centralized location in the scan, in this case a dynamically simulated pattern taken from the first band of strain-free silicon—and kinematically and dynamically simulated patterns. The original silicon lattice structure (space group 227) was used as the basis for generating the dynamically simulated reference patterns.

Even though creating an arbitrarily strained dynamically simulated lattice is impractical, it may be possible to achieve good results by creating a set of EMsoft libraries of the reference material at various strain states and using the strain state closest to the experimental image as the reference library. To test the effectiveness of this approach, the simulated scans used previously were analyzed again, using the tetragonal libraries used to generate the patterns to also generate the reference patterns. To calculate the absolute strain, the reference deformation tensor was created using the relationships established above:

$$F_{\text{ref}} = \begin{bmatrix} 1 - \frac{\epsilon_{\text{tet}}}{2} & 0 & 0 \\ 0 & 1 - \frac{\epsilon_{\text{tet}}}{2} & 0 \\ 0 & 0 & 1 + \frac{\epsilon_{\text{tet}}}{2} \end{bmatrix}. \quad (10)$$

The absolute deformation tensor was then calculated by multiplying the reference deformation tensor by the relative deformation tensor of the cross-correlation.

## RESULTS AND DISCUSSION

### HR-EBSD Analysis with Different Reference Pattern Types

The accuracy and precision of the HR-EBSD analyses across the  $\text{Si}/\text{Si}_{1-x}\text{Ge}_x$  scans, for different reference pattern types, are listed in Table 3 and plotted in Figure 4. The results showed that in all cases dynamical patterns are more precise than kinematical patterns, with a 50–90% decrease in standard deviation in both silicon and silicon germanium sections. Dynamical patterns improved the accuracy of the tetragonality measurement in the strain-free silicon for both scans; however, the relative accuracy of the dynamical versus kinematical patterns when measuring the tetragonality in the silicon germanium was different for both samples.

As shown in Figure 4, both the SSE and standard deviation of the silicon germanium was larger than those of the silicon for kinematical reference patterns. This is most

**Table 3.** Accuracy (Summed Squared Error, SSE) and Precision (SD) of High-Resolution Electron Backscatter Diffraction Analyses with Different Reference Pattern Types.

Scan	Reference Pattern	Si		Si <sub>1-x</sub> Ge <sub>x</sub>	
		SD	SSE	SD	SSE
S01	Real	0.019	0.003	0.023	0.004
S01	Kinematical	0.286	0.101	0.231	0.056
S01	Dynamical	0.058	0.007	0.046	0.003
S01	Dynamical-single	0.051	0.006	0.040	0.003
i02	Real	0.034	0.017	0.034	0.001
i02	Kinematical	0.203	0.061	0.127	0.040
S01	Dynamical	0.065	0.007	0.063	0.052
i02	Dynamical-single	0.042	0.010	0.054	0.026

likely due to the inherent bias placed upon the silicon germanium during PC calibration. As many different PC calibrations were performed, the ones with the lowest SSE in the silicon germanium were selected, whereas others had lower SSE values of the silicon. Despite this, the PC selected had sufficiently low SSE in the silicon to not cause significant concern as to the validity of the comparison in this study.

Figure 5 shows the results for the 1.25% tetragonal S01 scan using experimental, kinematic, and dynamical reference images, from top to bottom, respectively. The measured tetragonality is plotted on the left, with the expected tetragonality for the Si<sub>1-x</sub>Ge<sub>x</sub> from Vaudin et al. shown as a dashed line. The measured individual strain components are shown on the right. The near-zero strain in the Si for all three reference image types is indicative of a good PC calibration. The decrease in noise using dynamical instead of kinematical patterns is clearly shown, as well as the comparable accuracy for all three reference image types.

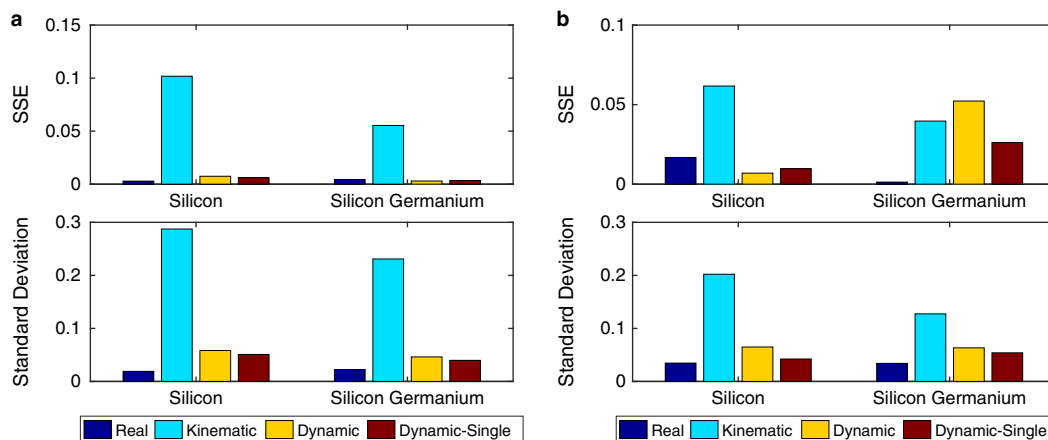
Figure 6 shows the results for the 2% tetragonal i02 scan, exhibiting a similar decrease in noise using dynamical patterns. However, the measured tetragonality in the Si<sub>1-x</sub>Ge<sub>x</sub> when using dynamical reference patterns is below the

expected value, and even slightly lower than that measured using kinematical reference patterns. This may be an indication that at higher values of tetragonality, the ability of the kinematical patterns to adjust the hypothetical lattice to incorporate the distortion may give it a slight advantage. To investigate the effect of increasing tetragonality on the accuracy of using dynamical reference patterns, several simulated scans were generated with increasing levels of tetragonal strain, as described in the Impact of Simulating a Deformed Lattice section, with results discussed below. The spike in the strain and tetragonality shown in Figure 6 for the dynamically simulated reference patterns is due to a poorly indexed point that was unable to be resolved. A similar but smaller jump is also noticed in the results using real patterns. As this point is at the transition between silicon and silicon germanium, it was not considered significant to the purpose of the comparison and was not analyzed in any greater depth.

It was hypothesized that part of the reason for lower noise levels (or higher precision) when using the real reference pattern relates to the fact that all patterns in the scan are compared with a single reference pattern. Table 3 demonstrates that when a single dynamical pattern is used as the reference for the entire scan, the precision does in fact improve significantly in both the silicon and silicon germanium in both samples, with an average improvement of 18%. This suggests that using a single reference pattern within a single grain of a sample being analyzed may improve the precision of the results, although the accuracy may not be significantly affected. In a polycrystalline sample, a single reference pattern could be generated for each grain, but if there are significant changes in orientation within the grain, especially near grain boundaries, using a single reference pattern may decrease the accuracy of the analysis.

### Convergence of the Iterative Algorithm

As shown in Figure 7, the iterative algorithm used to improve the accuracy of the relative distortion calculation

**Figure 4.** Precision (SD) and accuracy (summed squared error, SSE) of high-resolution electron backscatter diffraction analysis with different reference pattern types for the S01 (a) and i02 (b) scans.



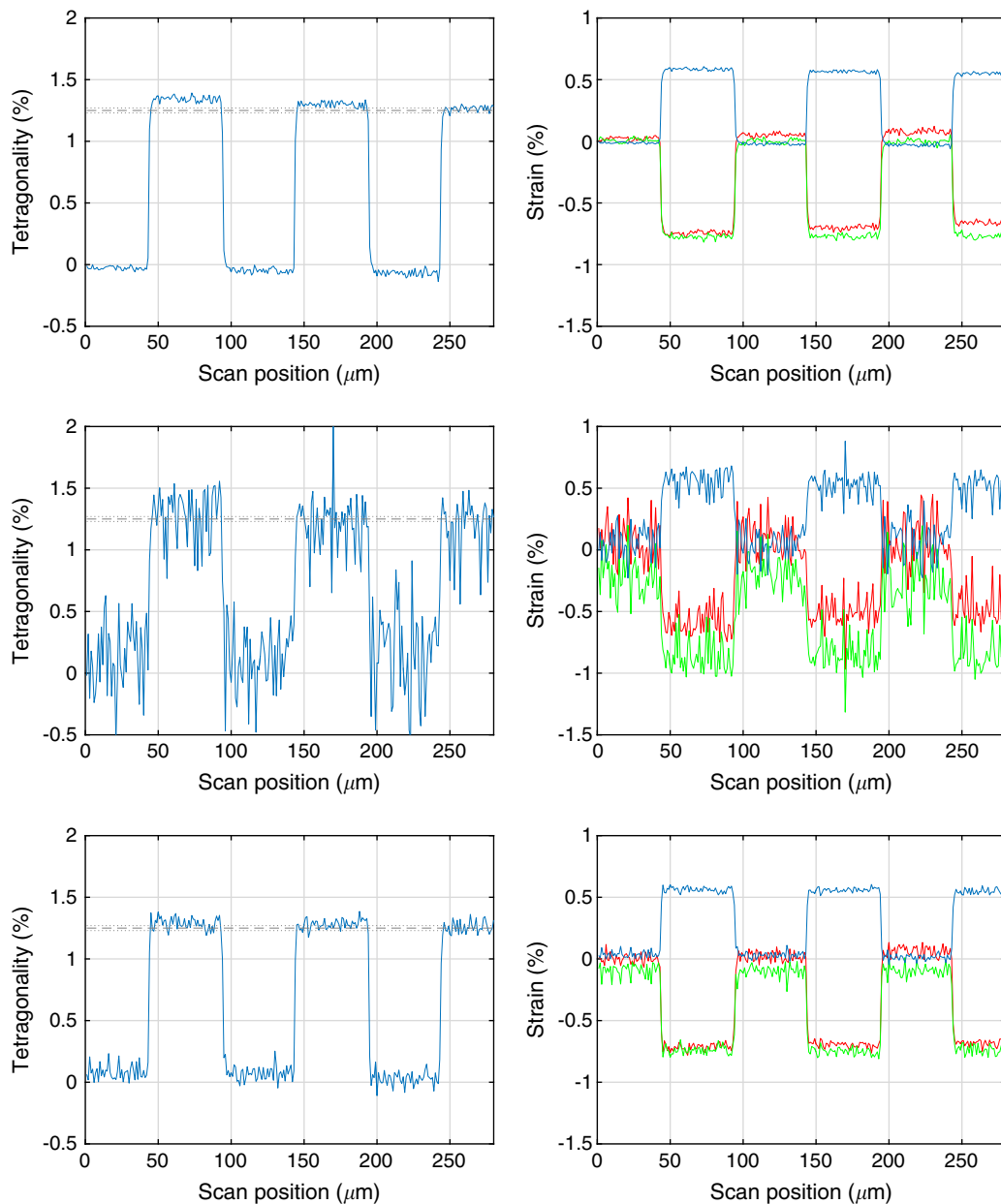


**Figure 5.** S01 sample high-resolution electron backscatter diffraction analysis results for experimental (top row), kinematically simulated (middle row), and dynamically simulated (bottom row) reference patterns. Measured tetragonality (left column) is plotted, with the expected tetragonality from Vaudin et al. (2015) shown by a dashed line. The individual strain components (right column)  $\epsilon_{11}$ ,  $\epsilon_{22}$ , and  $\epsilon_{33}$  are shown in red, green, and blue, respectively.

between experimental and reference lattices when using simulated reference patterns converged within a few iterations. The plots on the left show that the cross-correlation coefficient [equation (3)] increases as the algorithm progresses, signifying that the images align better on a pixel-to-pixel basis, and that this correlation converges on a specific value. The middle plot, shift magnitude, measures the differences in the SSE of the shifts between the two lattices (the SSE of the shifts for each ROI are represented by the lengths of the lines in Fig. 2). As expected, this value decreases to 0 as the shifts between successive iterations become very small and the algorithm

converges on a relative distortion tensor. The right plot shows the convergence of the error in accuracy of the tetragonality measurement, which also converges to 0, indicating the algorithm not only converges but converges on the correct value.

The top row are plots of the convergence for the algorithm with kinematical reference patterns, which have two steps in the iterative process: the first corrects only the orientation of the simulated reference pattern, and the second corrects both strain and orientation. The separation between these two steps is indicated by the vertical dashed line. As shown, the kinematical patterns did not converge

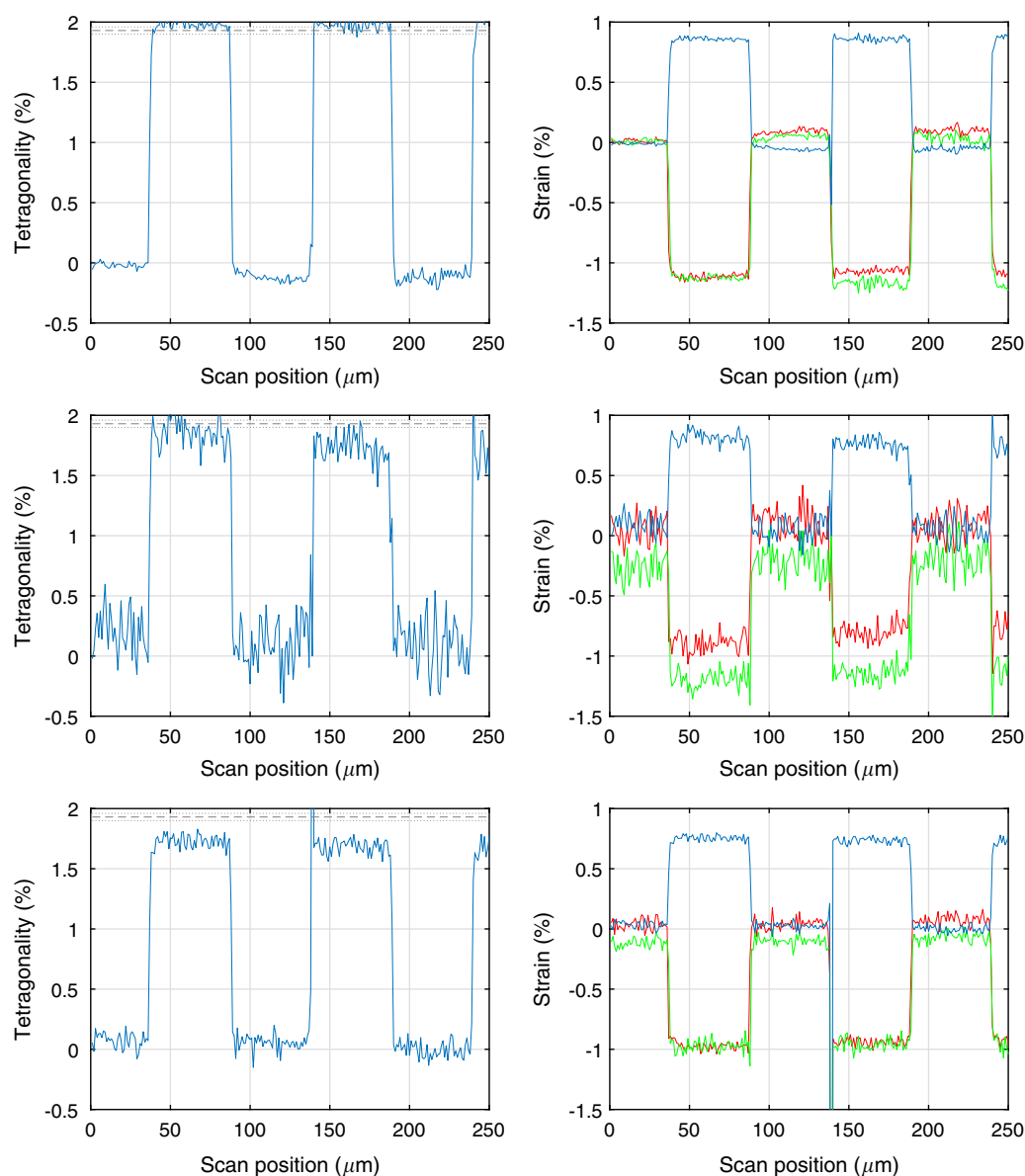


**Figure 6.** i02 sample high-resolution electron backscatter diffraction analysis results for experimental (top row), kinematically simulated (middle row), and dynamically simulated (bottom row) reference patterns. Measured tetragonality (left column) is plotted, with the expected tetragonality from Vaudin et al. (2015) shown by a dashed line. The individual strain components (right column)  $\varepsilon_{11}$ ,  $\varepsilon_{22}$ , and  $\varepsilon_{33}$  are shown in red, green, and blue, respectively.

well when correcting only the orientation of the reference pattern, whereas the dynamical converged on the correct value even though no strain was included in the reference pattern. However, the kinematical patterns converge quickly to the correct value once strain is included. This shows that the higher-fidelity dynamical patterns naturally converge better than kinematical patterns, but that the ability of the kinematical patterns to include strain in the reference pattern with no detrimental effects on performance allows the kinematical patterns to converge just as well as the dynamical patterns.

After extending out all iteration limits for both types of patterns (20 for kinematical, ten for dynamical) it was found

that kinematical patterns converged after five orientation-only iterations and six strain-and-orientation iterations (for 11 total orientations), and that dynamical patterns converged after six orientation-only iterations. Given that kinematical patterns can be generated about 40% faster than dynamical patterns (in the current configuration), the total calculation time for these recommended limits makes the algorithm for dynamical patterns about 1 s faster than kinematical patterns (about 10 s in total). These limits are the recommended limits for the given material, but may require adjustment based upon factors such as the quality of patterns, accuracy of the strain calculations of the scan software, and PC error. It was found that changing these

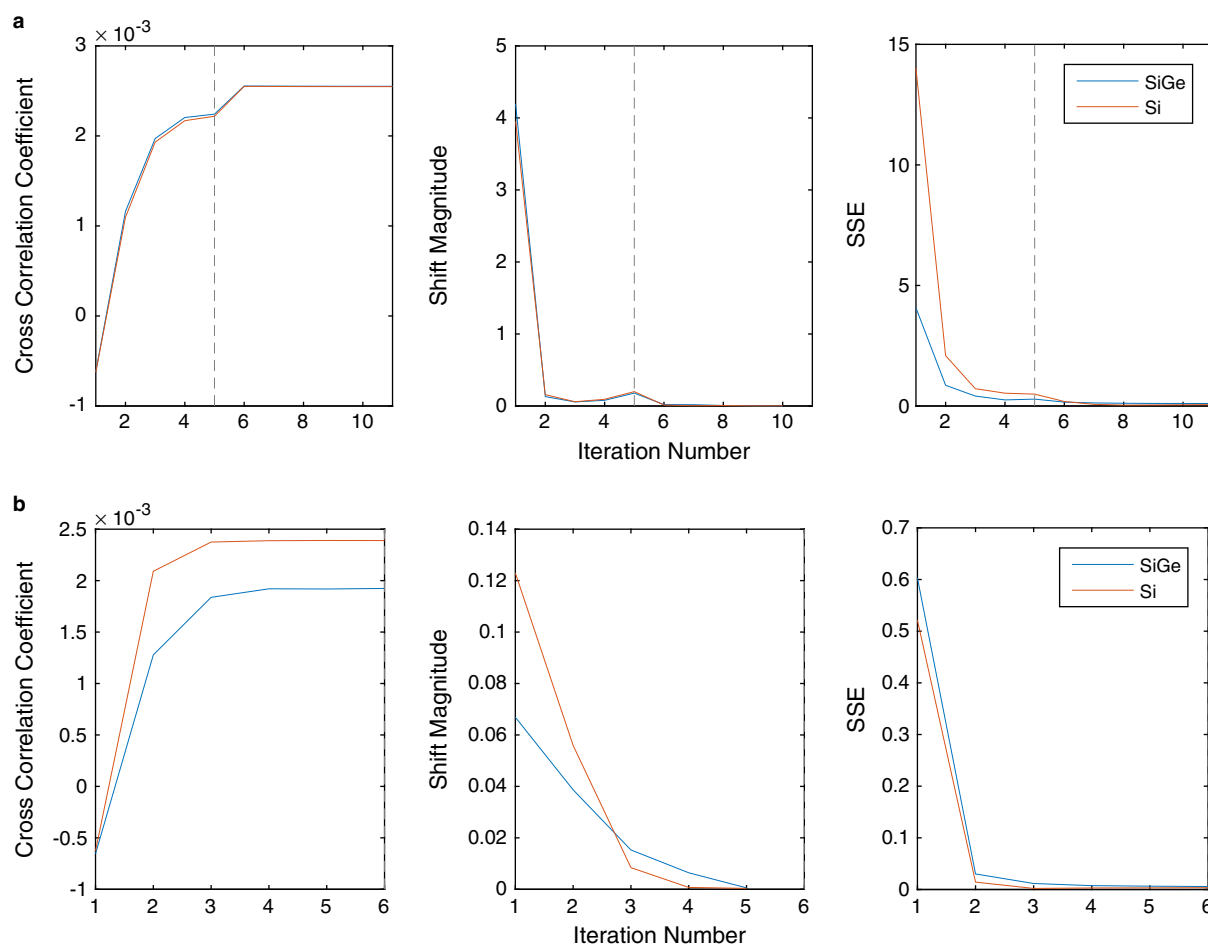


**Figure 7.** Convergence of iterative algorithm measured by cross-correlation coefficient (left), shift magnitude (middle), and accuracy of tetragonality measurement, or summed squared error (SSE) (right) for S01 scan. (a) Kinematical and (b) dynamical reference patterns.

limits by one or two iterations did not have significant effect on the accuracy and precision of the tetragonality calculation. The limits are suggested based on the approximate error of the SSE of the tetragonal strain dropping below a threshold value of 10%.

### Impact of Simulating a Deformed Lattice

As discussed earlier, in this section we wish to determine the effect of using a reference pattern from an undeformed lattice to characterize a significantly deformed lattice; further, we wish to assess the advantage of allowing the lattice of the reference pattern to deform to match the lattice being characterized. A series of simulated scans with 1–5% tetragonality were generated as described in the Impact of Simulating a Deformed Lattice section. The lattice parameters used to generate the required level of tetragonality are recorded in Table 4. Three reference pattern types were used: a “real” reference pattern (meaning an undistorted pattern taken from the simulated set of scan patterns), dynamical reference patterns (simulated with cubic symmetry, but with the ability to be rotated to better match the orientation of the

simulated scan patterns), and kinematical patterns (initially simulated with cubic symmetry, but subsequently allowed to distort to better match the lattice characteristics of the simulated scan patterns). To ensure good convergence, the kinematical patterns were run with six rotation-only iterations and six strain-and-rotation iterations, and the dynamical patterns were run with six rotation-only iterations.

The results of the comparison are shown in Figure 8. Above 2% tetragonality the error in the measurement of tetragonality increases significantly with dynamical reference patterns with cubic lattice symmetry, whereas the error of the kinematical patterns remains low even at high levels of tetragonality because of the ability of this approach to deform the reference lattice to match the experimental lattice. Therefore, above an approximate threshold value of 2% tetragonality, the use of a closely matched kinematically simulated tetragonal reference lattice results in a more accurate measurement of absolute strain than the dynamically simulated cubic lattice. The “real” pattern performed better than the default dynamical approach as the real reference pattern has the correct orientation to start with, and hence cannot confuse orientation error with distortion error.

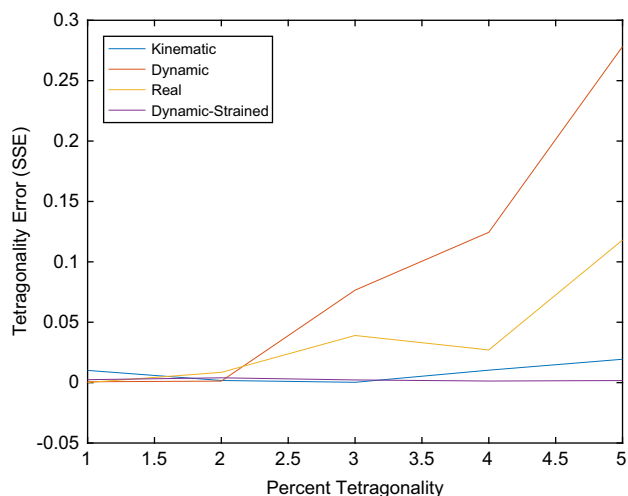
**Table 4.** Lattice Parameters for Varying Levels of Tetragonality.

Tetragonality	0%	1%	2%	3%	4%	5%
$a_{\text{SiGe}}$	3.840	3.821	3.802	3.783	3.763	3.744
$c_{\text{SiGe}}$	5.431	5.458	5.485	5.512	5.540	5.567

Units in Å.

Overall, at high levels of tetragonality the ability of the kinematical patterns to better replicate the pattern in terms of band placement overcomes the advantages of the higher-fidelity dynamical patterns. However, at low levels of strain the kinematical patterns did significantly worse than the dynamical patterns. This suggests two potential improvements to the dynamical reference pattern method. First, if the material is known to be tetragonal, master dynamical patterns could be created with levels of tetragonality ranging in steps of <2%, and the search for the best reference pattern could draw from these different possible databases. Alternatively, it would be possible to use kinematical patterns to approximate the absolute strain, and then generate an MC and master EBSD simulation for the material with a deformed lattice that closely resembles the experimental patterns for given sample or grain using the calculations from the kinematical patterns. This hybrid approach would be time intensive but may yield the best results in terms of both accuracy and precision.

To investigate the viability of the first improvement and further analyze the impact of using a deformed reference pattern, reference patterns were generated from the same master EBSD used to generate the original images. As the absolute deformation tensor of these patterns is precisely known, the absolute deformation tensor of the scan pattern was calculated by multiplying the relative distortion tensor from the cross-correlation by the absolute deformation tensor of the reference pattern. The results are plotted as the “dynamic-strained” entry in Figure 8. As shown, this

**Figure 8.** Effect of increasing tetragonality on accuracy.

approach worked better than using kinematical patterns, and had a similar computation time. However, as there was almost 0 relative distortion between the experimental and reference images, these results represent the theoretical limit of performance using this method. The worst case will likely occur when the actual tetragonality is halfway between steps of tetragonality. As it has been shown that dynamical patterns still performed significantly better than kinematical patterns when analyzing the S01 scan at 1.25% tetragonality, the dynamical patterns should still perform much better than the kinematical patterns at the worst case of this method. Therefore, to achieve accurate and precise tetragonality measurements using dynamically simulated reference patterns for materials with high tetragonal distortion, a library of master EBSD can be generated with spacing of about 1% tetragonality for comparison with the real patterns. As the tetragonality of these scans was known, the master EBSD with a matching level of tetragonality was selected manually; however, in experimental patterns where the tetragonality is unknown, a strain-free pattern would be generated first, which would be cross-correlated with the experimental pattern to determine an approximate level of tetragonality. This approximate tetragonality would then be used to index into the library of available levels of tetragonality, from which the closest matching master EBSD would be selected. Although yet untested, theoretically this approach could be used to accurately determine the absolute strain of a sample of unknown levels of high tetragonality. Although the initial generation of the library will be extremely time intensive as an MC and master EBSD simulation must be performed for every level of tetragonality, once the library is created there should be little to no cost in computation when using this approach. Future studies may show the effectiveness of this approach.

For both kinematically and dynamically simulated reference patterns, it has been shown that the accuracy of the strain, and therefore tetragonality, measurements is significantly affected by the amount of relative strain between the two images. Results can be significantly improved by simulating a reference image that closely resembles the experimental image in both orientation and deformation.

## CONCLUSION

Comparisons between kinematically and dynamically simulated EBSD reference patterns using a standard material showed that the higher-fidelity dynamical patterns significantly reduced variation or “noise” in the measurement of tetragonality in a standard material by 50–90%. At low levels of lattice distortion, dynamical patterns were both more precise and accurate than kinematical reference patterns; however, at higher levels of tetragonality the accuracy of the dynamical patterns dropped off, because they were computed based on an undistorted unit cell, and kinematical patterns resulted in better measurement of tetragonality. Although the dynamically simulated patterns show great promise as reference patterns for HR-EBSD



analysis, kinematical patterns continue to offer the distinct advantage of easily including strain within the reference lattice, allowing the reference pattern to closely resemble the experimental pattern even at high levels of lattice distortion. When the sample material has a reasonably low level of distortion, dynamically simulated reference patterns will give better results than kinematical images, and comparable accuracy and precision to experimental patterns, with the additional benefit of absolute strain determination (assuming that an accurate PC can be found). When significant lattice distortion exists within the sample (e.g., above 2% tetragonality), kinematical patterns may be the better choice if absolute strain calculation is required; alternatively, a library of dynamically simulated patterns may be compiled at various discrete steps of tetragonality to serve as reference patterns. It has been shown that by using several libraries of dynamical images with step sizes of about 1% tetragonality, dynamical results can very accurately calculate high levels of tetragonality within a scan. This approach shows great promise and further studies should validate this approach using experimental methods rather than the simulated methods used in the current study.

Once the initial MC and master pattern simulations have been completed for dynamical patterns, both types of simulated patterns result in similar HR-EBSD computation times. However, future development of dynamical patterns and careful integration into HR-EBSD analysis tools may drastically reduce the time required to extract a pattern from the master library, at which point dynamical patterns will provide faster, more accurate, and more precise HR-EBSD analysis than kinematical patterns.

PC error continues to be a significant setback when using simulated patterns. However, the strain-minimization technique used in the current study effectively minimized the error and accurate results were found using both kinematical and dynamical reference patterns. The calibration proved to be repeatable over a wide range of orientations. Some discrepancy was found between the calibrated PC for kinematical and dynamical patterns, which may be due to inherent differences in the two approaches, resulting in different band profiles and contrast. Further research may explain these differences, as well as provide better methods for accurate and repeatable PC determination.

The iterative approach used in the cross-correlation algorithm to determine the relative distortion between experimental and simulated reference patterns converged within four to six iterations for both kinematically and dynamically simulated reference patterns. It was shown that the ability to distort the lattice in the iterative algorithm significantly improved the accuracy of the measurement of the tetragonality.

## ACKNOWLEDGMENTS

The BYU team was supported by US Department of Energy, Office of Science, Basic Energy Sciences, under Award No. DE-SC0012587. The CMU authors wish to acknowledge an

Air Force Office of Scientific Research MURI program (contract no. FA9550-12-1-0458) as well as the Materials Characterization Facility at CMU under grant no. MCF-677785. The authors thank Mark Vaudin and NIST for the valuable experimental data.

## REFERENCES

- ALKORTA, J. (2013). Limits of simulation based high resolution EBSD. *Ultramicroscopy* **131**, 33–38.
- BASINGER, J., FULLWOOD, D., KACHER, J. & ADAMS, B. (2011). Pattern center determination in EBSD microscopy. *Microsc Microanal* **17**, 330–340.
- BIGGIN, S. & DINGLEY, D. (1977). A general method for locating the X-ray source point for Kossel diffraction. *J Appl Crystallogr* **10**, 376–385.
- BRIGHAM YOUNG UNIVERSITY (2015). OpenXY. Available at <https://github.com/byu-microstructureofmaterials/openxy> (retrieved May 17, 2015).
- BRITTON, T., MAURICE, C., FORTUNIER, R., DRIVER, J., DAY, A., MEADEN, G., DINGLEY, D., MINGARD, K. & WILKINSON, A. (2010). Factors affecting the accuracy of high resolution electron backscatter diffraction when using simulated patterns. *Ultramicroscopy* **110**, 1443–1453.
- BRITTON, T. & WILKINSON, A.J. (2012). High resolution electron backscatter diffraction measurements of elastic strain variations in the presence of larger lattice rotations. *Ultramicroscopy* **114**, 82–95.
- CALLAHAN, P. & DE GRAEF, M. (2013). Dynamical EBSD patterns part I: Pattern simulations. *Microsc Microanal* **19**, 1255–1265.
- DEAL, A., HOOGHAN, T. & EADES, A. (2008). Energy-filtered electron backscatter diffraction. *Ultramicroscopy* **108**, 116–125.
- DE GRAEF, M. (2015). Emsoft 3.0. Available at <http://www.github.com/marcdegraeef/emsoft> (retrieved December 12, 2015).
- FULLWOOD, D., VAUDIN, M., DANIES, C., RUGGLES, T. & WRIGHT, S. (2015). Validation of kinematically simulated pattern HR-EBSD for measuring absolute strains and lattice tetragonality. *Mater Charact* **107**, 270–277.
- GARDNER, C.J., ADAMS, B.L., BASINGER, J. & FULLWOOD, D.T. (2010). EBSD-based continuum dislocation microscopy. *Int J Plasticity* **26**, 1234–1247.
- THE HDF GROUP (2014). <http://www.hdfgroup.org/> (retrieved December 12, 2015).
- HUMPHREYS, C. (1979). The scattering of fast electrons by crystals. *Rep Prog Phys* **42**, 1825–1887.
- JOY, D. (1995). *Monte Carlo Modeling for Electron Microscopy and Microanalysis*. USA: Oxford University Press.
- KACHER, J., BASINGER, J., ADAMS, B.L. & FULLWOOD, D.T. (2010). Reply to comment by Maurice et al. in response to “Bragg’s law diffraction simulations for electron backscatter diffraction analysis”. *Ultramicroscopy* **110**, 760–762.
- KACHER, J., LANDON, C., ADAMS, B.L. & FULLWOOD, D. (2009). Bragg’s law diffraction simulations for electron backscatter diffraction analysis. *Ultramicroscopy* **109**, 1148–1156.
- LANDON, C., ADAMS, B. & KACHER, J. (2008). High resolution methods of characterizing mesoscale dislocation structures. *J Eng Mater Technol* **130**, 021004–021008.
- MAURICE, C., DZIECIOL, K. & FORTUNIER, R. (2011). A method for accurate localisation of EBSD pattern centres. *Ultramicroscopy* **111**, 140–148.

- MAURICE, C., FORTUNIER, R., DRIVER, J., DAY, A., MINGARD, K. & MEADEN, G. (2010). Comments on the paper "Bragg's law diffraction simulations for electron backscatter diffraction analysis" by Josh Kacher, Colin Landon, Brent L. Adams and David Fullwood. *Ultramicroscopy* **110**, 758–759.
- MINGARD, K.P., DAY, A.P. & QUESTED, P.N. (2014). Recent developments in two fundamental aspects of electron backscatter diffraction. *IOP Conf Ser Mater Sci Eng* **55**, 012011.
- RICE, K., KELLER, R. & STYKOVICH, M. (2014). Specimen-thickness effects on transmission Kikuchi patterns in the scanning electron microscope. *Microscopy* **254**, 129–136.
- ROŞCA, D. & DE GRAEF, M. (2013). Area-preserving projections from hexagonal and triangular domains to the sphere and applications to electron back-scatter diffraction pattern simulations. *Model Simulation Mater Sci Eng* **21**, 055021.
- ROŞCA, D., MORAWIEC, A. & DE GRAEF, M. (2014). A new method of constructing a grid in the space of 3D rotations and its applications to texture analysis. *Model Simulation Mater Sci Eng* **22**, 075013.
- RUGGLES, T. & FULLWOOD, D. (2013). Estimation of bulk dislocation density based on known distortion gradients recovered from EBSD. *Ultramicroscopy* **133**, 8–15.
- SCHWARTZ, A.J., KUMAR, M., ADAMS, B.L. & FIELD, D.P. (2009). *Electron Backscatter Diffraction in Material Science*. New York: Springer.
- TROOST, K., SLUIS, P. & GRAVESTIJN, D. (1993). Microscale elastic-strain determination by backscatter Kikuchi diffraction in the scanning electron microscope. *Appl Phys Lett* **62**, 1110–1112.
- VAUDIN, M., OSBORN, W., FRIEDMAN, L., GORHAM, J., VARTANIAN, V. & COOK, R. (2015). Designing a standard for strain mapping: HR-EBSD analysis of SiGe thin film structures on Si. *Ultramicroscopy* **148**, 94–104.
- VILLERT, S., MAURICE, C., WYON, C. & FORTUNIER, R. (2009). Accuracy assessment of elastic strain measurement by EBSD. *J Microsc* **233**, 290–301.
- WILKINSON, A.J., MEADEN, G. & DINGLEY, D.J. (2006). High-resolution elastic strain measurement from electron backscatter diffraction patterns: New levels of sensitivity. *Ultramicroscopy* **106**, 301–313.
- WILKINSON, A.J. & RANDMAN, D. (2010). Determination of elastic strain fields and geometrically necessary dislocation distributions near nanoindentations using electron backscatter diffraction. *Philos Mag* **90**, 1159–1177.
- WINKELMANN, A. (2010). Principles of depth-resolved Kikuchi pattern simulation for electron backscatter diffraction. *J Microsc* **239**, 32–45.
- WINKELMANN, A., NOLZE, G., VOS, M., SALVAT-PUJOL, F. & WERNER, W. (2016). Physics-based simulation models for EBSD: Advances and Challenges, IOP Conference Series: Material Science and Engineering, vol. 109.
- WINKELMANN, A., TRAGER-COWAN, C., SWEENEY, F., DAY, A.P. & PARBOOK, P. (2007). Many-beam dynamical simulation of electron backscatter diffraction patterns. *Ultramicroscopy* **107**, 414–421.
- WRIGHT, S. (1993). A review of automated orientation imaging microscopy (OIM). *J Comput Assist Microsc* **5**, 207.
- WRIGHT, S. & NOWELL, M. (2008). High-speed EBSD. *Adv Mater Processes* **166**, 29–31.
- WRIGHT, S., NOWELL, M. & BASINGER, J. (2011). Precision of EBSD based orientation measurements. *Microsc Microanal* **17**, 406–407.